Cryo-EM structure of mouse TRPML2 in lipid nanodiscs

Xiaojing Song[1,‡], Jian Li[2,‡], Miao Tian[3,‡], Huaiyi Zhu[4], Xiaohui Hu[1], Yuting Zhang[1], Yanru Cao[3], Heyang Ye[2], Peter J. McCormick[5], Bo Zeng[6], Yang Fu[3,*], Jingjing Duan[4,*], and Jin Zhang[1,*]

From the [1]School of Basic Medical Sciences, Nanchang University, Nanchang, Jiangxi, China; [2]College of Pharmaceutical Sciences, Gannan Medical University, Ganzhou, China; [3]School of Medicine, Southern University of Science and Technology, Shenzhen, Guangdong, China; [4]Human Aging Research Institute, School of Life Sciences, Nanchang University, Nanchang, Jiangxi, China; [5]Centre for Endocrinology, William Harvey Research Institute, Barts and the London School of Medicine, Queen Mary University of London, London, United Kingdom; [6]Key Laboratory of Medical Electrophysiology, Ministry of Education & Medical Electrophysiological Key Laboratory of Sichuan Province, Institute of Cardiovascular Research, Southwest Medical University, Luzhou, Sichuan, China

Edited by Wolfgang Peti

In mammalians, transient receptor potential mucolipin ion channels (TRPMLs) exhibit variable permeability to cations such as Ca^{2+}, Fe^{2+}, Zn^{2+}, and Na^+ and can be activated by the phosphoinositide PI(3,5)P2 in the endolysosomal system. Loss or dysfunction of TRPMLs has been implicated in lysosomal storage disorders, infectious diseases, and metabolic diseases. TRPML2 has recently been identified as a mechanosensitive and hypotonicity-sensitive channel in endolysosomal organelles, which distinguishes it from TRPML1 and TRPML3. However, the molecular and gating mechanism of TRPML2 remains elusive. Here, we present the cryo-EM structure of the full-length mouse TRPML2 in lipid nanodiscs at 3.14 Å resolution. The TRPML2 homotetramer structure at pH 7.4 in the apo state reveals an inactive conformation and some unique features of the extracytosolic/luminal domain and voltage sensor-like domain that have implications for the ion-conducting pathway. This structure enables new comparisons between the different subgroups of TRPML channels with available structures and provides structural insights into the conservation and diversity of TRPML channels. These comparisons have broad implications for understanding a variety of molecular mechanisms of TRPMLs in different pH conditions, including with and without bound agonists and antagonists.

Transient receptor potential mucolipin ion channels (TRPMLs) have been reported to be involved in membrane trafficking, vacuolar pH regulation, exocytosis, autophagy, and cell homeostasis (1–8). TRPMLs play important roles both physiologically and pathologically in lysosomal storage disorders, metabolic diseases, cell migration, metastasis formation, and infectious diseases (9–12). A loss-of-functional mutation in TRPML1 causes neurodegenerative lysosomal storage disorder, human mucolipidosis IV, with visual and many other impairments (12–17), while the loss-of-functional mutation in TRPML3 results in murine variant-waddler phenotypes characterized, e.g., by hearing loss and pigmentation defects (18–20). The intestinal abnormalities and failure to thrive were observed as well in TRPML1 and TRPML3 comutated neonatal mice (21). However, the function of TRPML2 remains obscure, it has not been implicated in any human nor mouse disease phenotype to date. Recent studies suggest essential roles for TRPML2 in immune cell development, both innate and adaptive immune responses, tumor progression, and virus infection (22–25). TRPML2 may also have overlapping function with the TRPML1 channel in complementing certain phenotypic alterations in MLIV cells (18, 26). A recent study has suggested that TRPML2 act as an osmo/mechanosensitive endolysosomal ion channel on intracellular membranes, making it unique to its relatives TRPML1 and TRPML3 (27). High-resolution structures of TRPML1 and TRPML3 had been recently solved by cryo-EM. Hirschi, Zhou et al. presented the structure of a full-length TRPML3 channel from Callithrix jacchus and three distinct states structures of the TRPML3 channel from human (28, 29). Schmiege et al. reported two structures of full-length human TRPML1 in the closed state at pH 7.0 and open-state structures at pH 6.0 respectively (30). Chen et al. presented a mouse TRPML1 channel embedded in nanodiscs revealing the phosphatidylinositol 3,5-bisphosphate ($PI(3,5)P_2$) binding site and mechanism of ligand binding to pore opening (31, 32). Crystal structures of the tetrameric human TRPML2 extracytosolic/luminal domain (ELD) have been determined at pH 6.5 and 4.5, respectively, which revealed the ELD responses to the different pH values in recycling endosomes and lysosomes (33). Here we report a cryo-EM structure of mouse long TRPML2 isoform in the apo-state (pH 7.4) at 3.14 Å resolution. Compared with the currently available TRPML1 and TRPML3 structures, the TRPML2 shows similar overall architecture with several key unique features, which provide structural characteristics of full-length TRPML2. Our current work contributes to a better understanding on the molecular details of TRPML subfamily members as well as providing new insights into their common and unique functions.

‡ These authors contributed equally to this work.
* For correspondence: Jin Zhang, zhangxiaokong@hotmail.com; Jingjing Duan, duan.jingjing@ncu.edu.cn; Yang Fu, fuy@sustech.edu.cn.

Results

Overall structure of TRPML2 in lipid nanodiscs

We fused the full-length mouse TRPML2 (mmTRPML2) construct with the maltose-binding protein (MBP) added to the N terminus and expressed it in the Bac-Bac expression system. Due to the cleavage of the MBP tag, we observed significantly impaired protein stability and reduced protein yield, thus we preserved this tag before single-particle cryo-EM structural determination. We purified full-length mmTRPML2(1–566a.a.) into lipid nanodiscs, generated with membrane scaffold proteins (MSP2N2) and soy extract polar lipids (Fig. S1, *A* and *B*). Calcium imaging experiments were performed to confirm that the MBP-TRPML2 construct used for cryo-EM possessed the same functional properties of wide-type TRPML2 (WT-TRPML2). A selective agonist of TRPML2 (ML2-SA1, 50 μM) (23, 34) induced increased cytoplasmic Ca^{2+} in both MBP-TRPML2 and WT-TRPML2-transfected HeLa cells, but no detectable increase was observed in the empty vector-transfected control cells (Fig. S1, *C* and *D*). SERCA2 is the major calcium pump in cells that may efficiently transport lysosome-released Ca^{2+} into the ER. Neither WT-TRPML2 nor MBP-TRPML2 overexpression affected the expression of SERCA2 (Fig. S1, *E* and *F*).

The cryo-EM images of frozen hydrated samples showed well-dispersed particles, some structural details of TRPML2 are visible in the two-dimensional class averages (Fig. S2, *A* and *B*), and the final three-dimensional reconstructed map displays a tetrameric assembly of channel subunits (Fig. S2*C*). Transmembrane helices were embedded within a disc-shaped density contributed by the nanodisc lipid bilayer that is located under an extracytosolic/luminal domain on a side-view 3D density map (Fig. 1, *A* and *B*). The full-length mmTRPML2 at pH 7.4 in lipid nanodiscs is determined at an overall resolution of 3.14 Å (PDB: 7DYS) (Figs. 1 and S3; Table S1). Some amino acids in the cytoplasm were not able to be modeled due to poor density, including the N-terminus (1–65a.a.), C-terminus (518–566a.a.), and S2-S3 regions (319–333a.a.).

The overall architecture of mmTRPML2 is similar to the previously reported TRPML1 and TRPML3 structures (28, 30, 31) and assembles in a symmetric homotetramer with 96 × 82 × 96 Å dimensions (Fig. 1, *B–D*). The ELD is a long luminal linker that contains seven β sheets and five extracytosolic helices (EH1–5), which is a feature of TRPML and TRPP subfamilies in TRP channels, also known as a "polycystin-mucolipin domain" (PMD). The ELD of each monomer subunit interacts with its neighbors forming a cap-like structure to the channel (Fig. 1*E*). The architecture of the TRPML2 transmembrane domain (TMD) is formed with an S1–S4 voltage sensor-like domain (VSLD), an S4–S5 linker, and an S5–S6 pore domain (Fig. 1, *E* and *F*). The pore loop in between of S5 and S6 is flanked by pore helices (PH1 and PH2). The N- and C- terminal domains exposed to the cytoplasm lack densities in our mmTRPML2 map, revealing their conformational flexibility. In view of the availability of full-length structures and similarity of purification conditions, we will mainly compare the current mmTRPML2

structure with mmTRPML1(PDB: 5YE5) and hsTRPML3 (PDB: 6AYE) hereafter.

The architecture of extracytosolic/luminal domain

The ELD is a feature of TRPMLs and TRPPs distinguishing from other TRP family members and contributes to the channel assembly, allosteric regulation, and channel gating (28, 35). The tetrameric ELD "cap" of mmTRPML2 (87–284a.a.) is located above the transmembrane domain. Each monomer contains five helices and seven-stranded anti-parallel β sheet (Figs. 1*F* and 2*A*). This architecture is stabilized by two disulfide bonds (Cys164 and Cys190; Cys243 and Cys274), which was shown previously in the study on TRPML2 ELD that two disulfide bonds are crucial for protein folding, but not for integrity of the fully folded protein (Fig. 2*B*) (33). Two hydrogen bonds are formed between Lys102-Ser118 and Leu104-Gln137, which connect the S1/EH1 and prepore loop (Fig. 2*C*). The Ser110 and Val112 in the prepore loop form the first restriction region for ion permeation along the center of the ELD tetramer, with the most restricted site formed by Val112 (Fig. 2*D*). Interestingly, compared with the ELD structures of hsTRPML2 at pH 6.5 (PDB: 6HRR) and pH 4.5 (PDB: 6HRS) (33), the ELD pore is more restricted in our current structure at pH7.4 (Fig. S4). Whereas in TRPML1 and TRPML3 (29, 36), the lower pH values induced more closed ELD pores. The observed ELD pore-size difference in the three conformations is likely due to the modifications of pH environment; however, the lack of TMD and cytosol domains may affect the size of human ELD structures (PDB: 6HRR and 6HRS), as well as the different analysis methods may also highlight the divergence. In TRPML2, a highly electronegative "tunnel" consists of the $^{113}DEDD^{116}$ tetramer in the prepore loop (Fig. 2*D*), which is the most acidic and negative-charged area among all TRPML channels (33) (see the alignment, Figs. S5 and S6). The S1 helix of mmTRPML2 extends extracellularly into ELD as a continuous α-helix, designated as EH1/S1. Such integrated helices form rigid connections between ELD and TMD, which may effectively propagate the conformational change from the luminal pore to the transmembrane domain and therefore regulate the ion channel activity. Although EH1/S1 helices of TRPML1-3 share many common features, there are differences in twist angles and lengths (Fig. S7). These regions in TRPMLs obviously are more compact than the corresponding architecture of PKDs. In addition, the EH1 of ELD and S1 of the transmembrane domain in PKD2 are linked with a short loop rather than forming a continuous α-helix in TRPMLs (Figs. 2*E* and S7) (35).

Structural features of voltage sensor-like domain

The VSLD can affect ion permeation through conformational changes. Similar to the TRPML1 and TRPML3, the S4 of mmTRPML2 is organized as an entirely α-helical conformation, in marked contrast with other TRP channels such as PKD2 that contains a 3_{10}-helix around the cytosol area (35, 37–39) (Fig. 3*A*). This rigid organization may serve as a
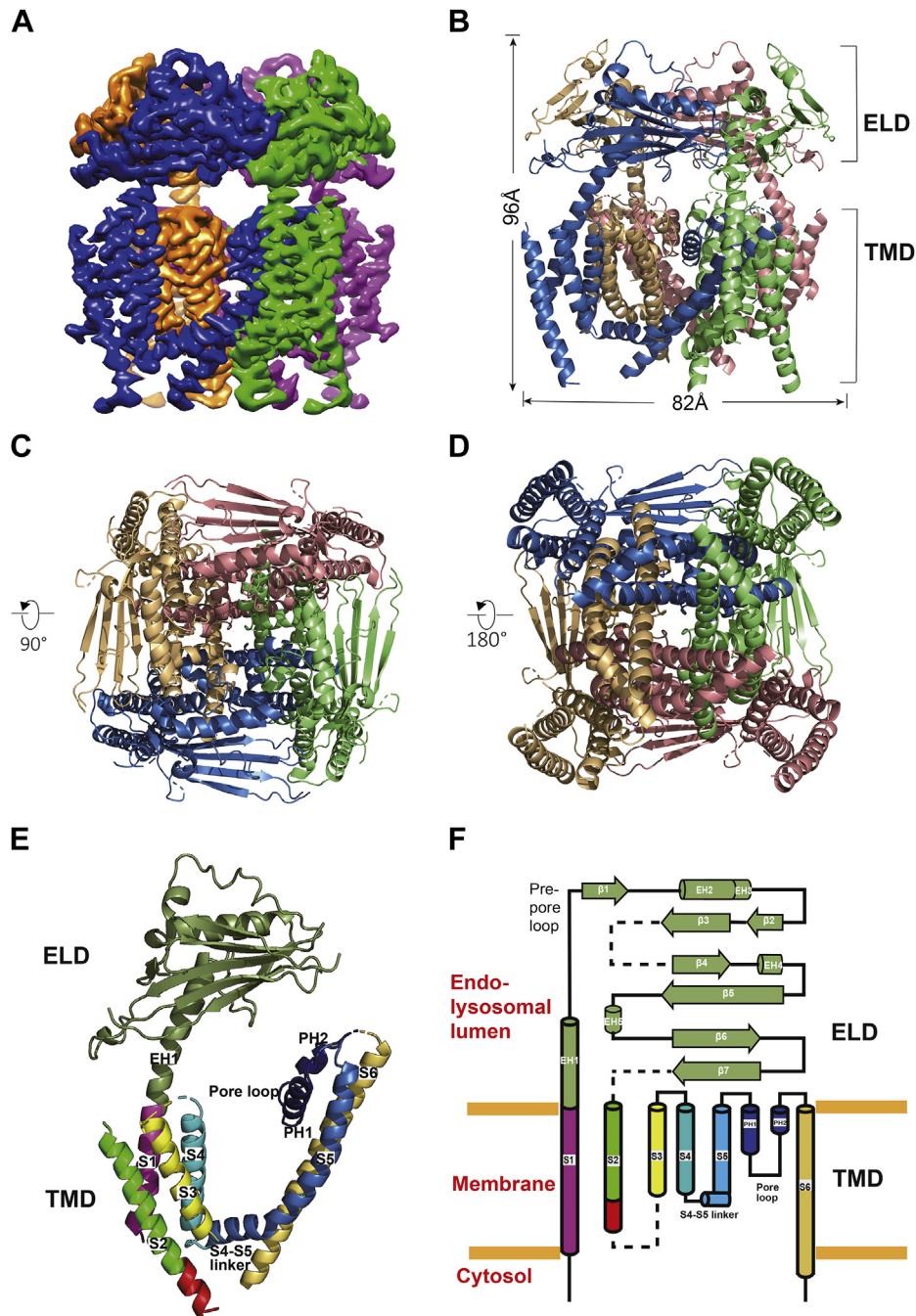
Figure 1. Overall structure of mouse TRPML2 channel (mmTRPML) determined in lipid nanodiscs. *A,* cryo-EM reconstruction density map of TRPML2 in a nanodisc. *B,* side view of a cartoon representation of TRPML2 homotetramer with dimensions labeled. Each channel subunit is color-coded individually. *Top C* and *bottom D,* views of mmTRPML2 structure. *E,* ribbon diagram depicting major structural domains of a single subunit. *F,* linear diagram depicting the structural details of a monomer, color-coded to match (*E*).

relatively stationary anchor coordinating with the S4–S5 linker movement to facilitate TRPML2 gating. Recent functional studies reveal the TRPML2 channel is an hypotonicity/mechanosensitive channel. Leu314 located in the cytosolic side of S2 is a crucial determinant for its hypotonicity sensitivity (27). The Leu314 is not conserved in TRPML1 and TRPML3, in which there are positively charged arginine residues instead (Fig. S5). Whereas another two amino acid residues, Arg395 and Tyr347, are conserved in TRPMLs that

are critical for PI(3,5)P$_2$-induced activation. At the predicted PIP$_2$-binding pocket of the mmTRPML2 structure, the Arg395 on the C-terminus of S4 interacts with side chains of Tyr347 and Trp346 on the S3 cytosolic interface *via* a hydrogen bond and a cation–π interaction, respectively (Fig. 3*B*). In the PIP$_2$-bound TRPML1 structures, the Tyr355, binding the 3′ phosphate group of PI(3,5)P$_2$, has cation–π interactions with arginine Arg403, thus allosterically affecting the S4–S5 linker to activate the channel (32).
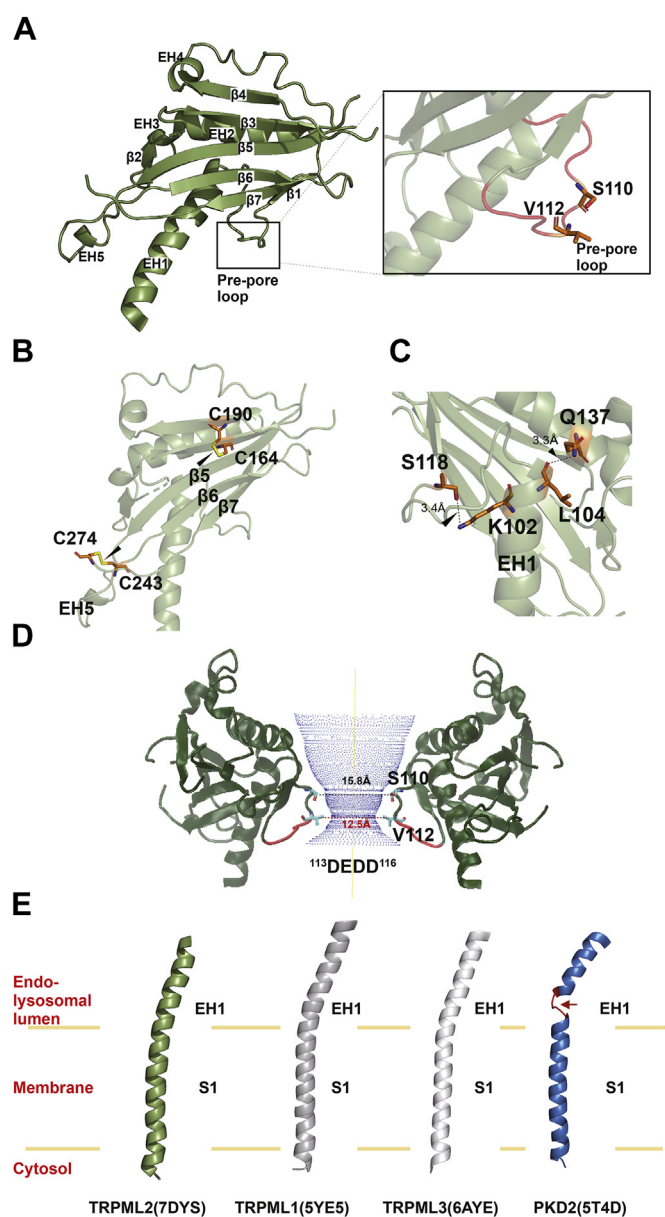
Figure 2. Structure features of the extracytosolic/lumenal domain (ELD) in mmTRPML2. *A*, ribbon diagram depicting a side view of ELD in mmTRPML2 and an enlarged view of prepore loop. *B*, two disulfide bridges found in ELD between Cys164 and Cys190, as well as Cys243 and Cys274, indicated by *arrows*. *C*, the interactions between ELD and EH1/S1 are indicated by *arrows*. *D*, a side view of the first restriction area of mmTRPML2 for ion permeation along the center of ELD shown as *dots* and mapped using HOLE. The narrowest point (12.5 Å) is at V112, followed by S110 as 15.8 Å between diagonally opposed residues. The acidic and negative-charged [113]DEDD[116] motif is labeled in *red* and indicated by *red arrows*. *E*, the continuous α-helix connecting ELD and transmembrane domain (TMD) in mmTRPML2 as EH1/S1 compared with mmTRPML1 (PDB: 5YE5), hsTRPML3 (PDB: 6AYE), and hsPKD2 (PDB: 5T4D).

Within each TRPML2 subunit, the S1–S4 and S5–S6 pore domains are connected by a helical S4-S5 linker that runs parallel to the inner leaflet of the lipid bilayer. Deformation and movement of the S4-S5 linker can affect the opening of the channel pore. The S4–S5 linker of mmTRPML2 adopting a short loop runs with a small straight helix connecting it with the S5 helix (Fig. 3C). The length of the loop in the S4-S5 linkers among TRPMLs is different. They are [398]GYFQ[401] of

mmTRPML2, [408]FHKY(N)[412] of mmTRPML1, and [396]AK[397] of hsTRPML3, respectively (Fig. 3*C*). It is interesting to note that the S4–S5 linker conformation of the mmTRPML1 at pH 8.0 (5WPV, 5WPT, and 5WPQ) (31) appears as a "loop-helix-loop" architecture differing from "loop-helixes" conformations of all other solved TRPML structures at neutral and acidic conditions. Unlike the S1 extending into the lysosomal lumen, the S2 protrudes into the cytosol, which connects cytosol linkers with transmembrane helices in the TRPML3 structure near the PIP$_2$-binding pocket (28). Due to poor density of the cytoplasmic region, only a part of the S2 cytoplasmic helical structure (310–319a.a.) is modeled in the current mmTRPML2 structure.

Structure of the ion permeation pathway

Similar to the other two TRPMLs, the ion conduction pathway of TRPML2 consists of three constriction regions, including a previously described vestibule entrance in ELD, a selectivity filter in the pore region, and a lower gate near the inner leaflet of the lipid bilayer (28, 30, 31, 33) (Fig. 4*A*). Since the current structure was determined in the absence of ligands (apo), the ion conduction pore consisting of the S5, S6, and two pore helices (PH1 and PH2) adopts a closed conformation (Fig. 4*B*). The outer pore region is notably rich with negatively charged residues, which may serve as a sink for accumulating cations and thus enhancing ion conduction (Fig. S6). The highly conserved [461]NGD[463] in the TRPML subfamily forms the selectivity filter of mmTRPML2, with backbone carbonyls pointing toward the central pore axis (Fig. 4*B*). In the extracellular region, the negatively charged Asp464 residues interacting with neighboring side chains mark a constriction of 5.9 Å between diagonally opposed residues (Fig. 4, *B* and *C*), which coordinate permeating cations, while repelling anions. Continuing down the pore, Ile503 in the S6 helix forms the cytosolic gate to prevent the passage of hydrated cations while the lower gate of TRPML2 is at its narrowest 4.5 Å between diagonally opposed residues (Fig. 4, *A* and *B*). The overall structures of the three TRPML channels are highly similar but still distinguished from each other. The selectivity filter size of TRPML2 is comparable among the three TRPML channels (5.5~5.9 Å); however, the lower gates of TRPML2 (4.5 Å) and TRPML3 (5.3 Å) are much tighter than that of TRPML1 (10.8 Å) (Fig. S8). Some highly conserved structural features among TRP channels are also detected in mmTRPML2 including π-helices formed by [494]FIYMV[498] in the middle of S6 (Fig. 4*B*) and side chain interactions between residues in PH1 and PH2 (Fig. 4, *D–F*), all of these cooperate to facilitate the ion permeation.

Discussion

TRPML2 is predominantly expressed in lymphocytes and other immune cells and has recently been identified as the only mechanosensitive channel in endolysosomal organelles (22, 27). TRPML2 has been reported to play a critical role in adaptive immunity, promoting the activation of macrophages and subsequent macrophage migration under LPS stimulation
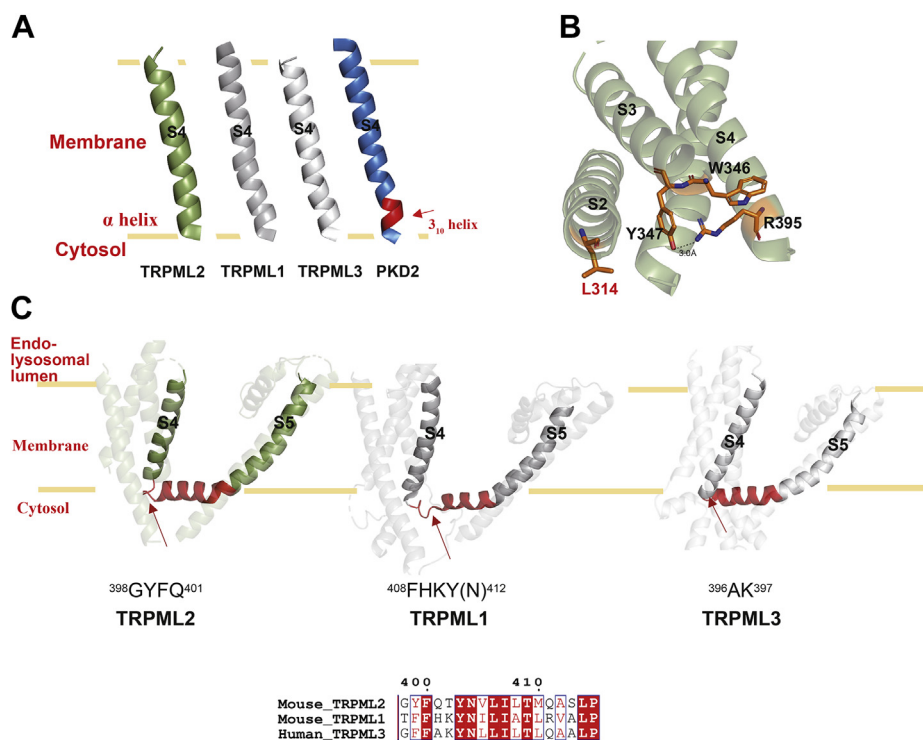
Figure 3. Structure features of the voltage sensor-like domain (VSLD) in mmTRPML2. *A,* the S4 helix of TRPML2 was compared with mmTRPML1 (PDB: 5YE5), hsTRPML3 (PDB: 6AYE), and hsPKD2 (PDB: 5T4D). In marked contrast with other TRP channels including PKD2, TRPML subfamily channels do not contain a 3_{10}-helix around the inner leaf of lipid bilayer. *B,* R395 of S4 at the cytoplasmic end is likely stabilized by aromatic and negatively charged residues Y347 and W346 of S3. Critical L314 for TRPML2 mechanosensitivity is nearby. *C,* the S4–S5 linker structure (labeled as *red*) of mmTRPML2 was compared with mmTRPML1 (PDB: 5YE5) and hsTRPML3 (PDB: 6AYE). The loop lengths and architectures of linkers are different among three TRPML channels.

(23). However, the detailed biological function and molecular mechanism of the TRPML2 channel remain elusive. Our mmTRPML2 structure in the apo state, obtained in lipid nanodiscs, which mimic the native cellular environment, will contribute to a deeper understanding of channel gating mechanisms and corresponding biological mutational effects. It is known that TRPMLs can be activated by ML-SA1 and endogenous PI(3,5)P$_2$, while can be inhibited by PI(4,5)P$_2$ and sphingomyelins (40–42). The extracellular/luminal pH, calcium, and other factors have also been reported to modulate the gating of TRPML channels (40, 43). Based on available reported structures and our novel finding, several potential mechanisms may mediate these responses in TRPML2. Firstly, the ELD under variable pH conditions at endosomes or lysosomes *in vivo* could affect TRPML2 conformation. The ELD forms a fenestrated canopy at the top of the channel gating and assembles into a highly negative electrostatic trap to facilitate attracting and directing of cations into the luminal pore, thus acting as an ion selection or guidance system. The ELD pore of TRPML1 in pH 4.5 appears narrower than in pH 6.0 and pH 7.5 (Fig. S9A, *upper*). The ELD of TRPML3 is in a closed state with an extremely restricted pore about 1 Å diameter in pH 4.8 rather than in pH 7.4 of which the most restricted site is at lower gate (Fig. S9A, *lower*). The ELD pore size of TRPML2 seemed more open under acidic conditions (pH 4.5 and pH 6.5) compared with that of the structure at pH 7.4 (Fig. 2E) (Fig. S9A, *middle*). The mouse full-length TRPML2 structure

reveals a more restricted ELD pore, which may be due multiple factors rather than pH effect alone, while this variation in ELD opening appears to be a distinctive feature for TRPML2 in the endolysosomal pathway. In some ways this makes sense as the ELD is exposed to the endolysosomal lumen, which has different Ca^{2+} concentrations and pH values, which in turn influence channel activity (29, 31, 33). The dual Ca^{2+}/pH regulation of TRPML2 is that the S110 and V112 forms a restriction pore closely above a highly electronegative ^{113}DEDD^{116} tetramer in the prepore loop, which attracts and binds to extracellular/lumen Ca^{2+}, thus blocking the conduction of Ca^{2+} and monovalent cations. At a lower pH, the protonation reduces the negative charge on the surface of ^{113}DEDD^{116} motif, thus weakening the blocking effect. Meanwhile, the restriction formed with S110 and V112 tetramer seemed wider for citations pass through (Fig. 2D). Secondly, The ML-SA1-binding pockets in TRPML1 and TRPML3 are found in a hydrophobic cavity close to the selectivity filter (Fig. S9B). This is formed by the aromatic and hydrophobic residues in PH1, S5, S6, and S6 from the neighboring subunit (30). The agonist ML-SA1 mainly acts on the lower gates of TRPML channels to induce the openings. In the case of TRPML2, ML2-SA1 is likely to bind to the same hydrophobic cavity interacting with Tyr347 and Arg395 in the ligand binding pocket. Thirdly, two kinds of PIP$_2$ lipids, agonist PI(3,5)P$_2$ and antagonist PI(4,5)P$_2$ interact with a tyrosine and an arginine on the extended helices of S1–S3 in
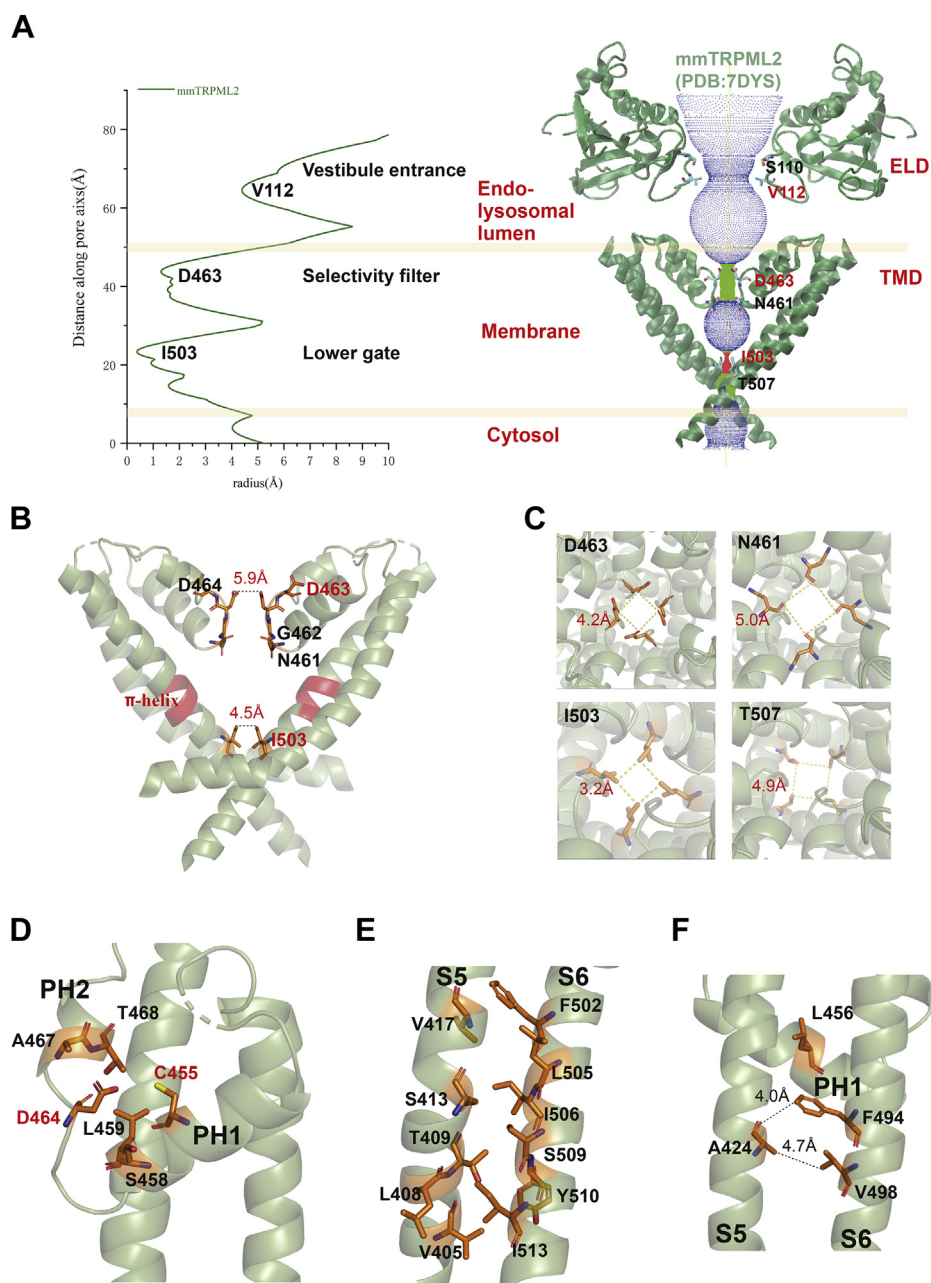
Figure 4. Ion conduction pathway and pore domain structure of the in mmTRPML2. *A,* pore sizes along the ion conduction pathway of mmTRPML2 was calculated (*left*) and shown as *dots* and mapped (*right*) using HOLE. The pathway is consisted with three restrictions: Vestibule entrance in ELD, selectivity filter below the outer leaflet and lower gate around the inner leaflet of lipid bilayer. The narrowest site of each restriction was at V112, D463, and I503, respectively. *B,* the atomic model of the pore domain in mmTRPML2. Two S5–S6 subunits are shown with atom–atom distances labeled between diagonally opposed residues as 5.9 Å (D463) and 4.5 Å (I503) with the π-helix in the *middle* of S6 is colored in *red*. *C,* the critical residues D463, N461, I503, and T507 for ion conduction and the distance with neighboring subunit were enlarged and labeled as shown. *D,* an interaction network couple C455 in pore helix 1 (PH1) and D464 in selectivity filter of one subunit with pore helix 2(PH2) and S6 of a neighboring subunit. *E,* the packing between S5 and S6 facilitates pore domain as closed state in apo. *F,* interactions from A424 in S5 to amino acid residues in S6.

the same binding pocket of hsTRPML1 (13, 32, 44) (Fig. S9*C*). Despite the functional regulation of the agonist PI(3,5)P$_2$ and antagonist PI(4,5)P$_2$ in reverse, both kinds of PIP$_2$s force the lower gate a wider opening compared with hsTRPML1 in apo state under pH7.0; however, the structure of PI(4,5)P$_2$-bound TRPML1 had a more restricted selectivity filter in a closed state compared with PI(3,5)P$_2$ bound at pH5.5 (Fig. S9*C*). Although the binding sites of ML-SA1 and PIP2 are different in TRPML structures, the combination of PI(3,5)P$_2$ and ML-SA1 regulated the lower gate to open to a similar extent as ML-SA1 alone (Fig. S9*C*). Based on these reported structures, we can speculate the medications of TRPML2 under variable physiological conditions with a similar dynamic mechanism in coordination with the mechanical force to regulate the pore size. Future studies should also bear in mind that there might be additional or different structural variations because the above comparisons were carried out in structures under various conditions.

TRPML2 channel has not been associated with human disease to date, and its physiological properties are poorly understood. It is worth noting that some experimental mutations offer clues for a better understanding of TRPML2 physiological functions. Mutagenesis of the acidic residues E114A, D115A, and D116A led to a dramatic loss in Ca^{2+} binding within the prepore loop ^{113}DEDD^{116} motif (Fig. 2A). Meanwhile, the Ca^{2+} interacts with this motif in a pH-dependent manner. The lower pH values in late endosomes or lysosomes enhance the protonation of the acidic ^{113}DEDD^{116} motif, subsequently weakening the Ca^{2+} binding (33). Sequence alignment in TRPML family shows that the 314 site of TRPML2 is leucine instead of arginine at the corresponding positions of TRPML1 and TRPML3 (Fig. S5, highlighted in *yellow*). An L314R mutation in TRPML2 specifically impairs the responsiveness to changes in cytosolic osmolarity but does not affect principal activation gating (27). Osmotic pressure can rapidly increase the level of PI(3,5)P$_2$ and subsequently activate osmo-mechanosensitive channels (27, 33). The negatively charged PI(3,5)P$_2$ may prefer to interact with positively charged arginine than uncharged leucine *via* a hydrophobic side chain. In PI(3,5)P$_2$-bound TRPML1 structure (PDB: 6E7P), the interactions between PIP$_2$ with R322 and other residues in IS1b and IS1a made a compact organization that could cage PIP$_2$ from release and made the structure less elastic. The corresponding PIP$_2$-binding pocket in our unligand-TRPML2 structure was in poor resolution that unfortunately cannot provide too much information on how the Leu314 in the cytosol region of S2 facilities the TRPML2 as a key channel in immune cells by virtue of its osmo/mechano sensitivity, whereas the poor resolution hints at a loose organization and the flexibility of this region in TRPML2 (Fig. S10). The obtaining of structures of TRPML2-PI(3,5)P$_2$ complex and L314 R mutation in TRPML2 with related functional tests are needed for further insights. A396P mutation of TRPML2 (isoform 2) exhibited an active state with an marked elevated $[Ca^{2+}]^i$ when compared with wild-type isoform (26, 45–47). Similarly, the corresponding site A424P mutant of mmTRPML2 (isoform 1) was still actively able to conduct Ca^{2+}, but may cause cell degeneration in mice and cells (47–50). These evidences reveal that these two alanine residues are physiologically important for stabilizing TRPML2 channel in the closed state in the apo structure. The G425A mutant was found to abrogate the activation effect of ML2-SA1 on TRPML2(23). In our mmTRPML2 structure, Ala396 is located in the end of S4 close to the loop of S4–S5 linker (Fig. 3C), while Ala424 and Gly425 are in the middle of S5 interacting with S6. The Cα-Cα distances in between of A424 in S5 and F494 and in between of Ala424 and Vla498 are 4.0 Å and 4.7 Å, respectively (Fig. 4F), facilitating interactions between S5 and S6 to maintain the TRPML2 channel in a closed state. The I367T, F457L mutations expressed in S2 cells did not affect the current amplitudes; however, the D463K/D464K mutation completely blocked the TRPML2-dependent current electrophysiologically (49) (Fig. S11). Our structure explains these findings as we observe these two Asp residues form the restriction site in the selectivity filter (Fig. 4B).

In summary, our full-length mmTRPML2 structure enables new comparisons between the different subgroups of the available TRPML channels. Our findings provide key structural insights into conservation and divergence of TRPML channels and have broad implications for understanding the diverse regulation mechanisms and functions of the large superfamily of TRP ion channels.

Experimental procedures
Protein expression, purification, and nanodiscs reconstitution

The full-length mouse TRPML2 (mmTRPML2, NCBI Reference Sequence: NM_026656.5) was cloned into the pEGBacMam vector with an MBP tag in N terminus for affinity purification with amylose resin (New England Biolabs). HEK293S GnTI$^-$ [from the American Type Culture Collection (ATCC)] cells were transduced with 10% (v/v) P4 baculovirus at a density of 2.0–3.0 × 10^6 cells/ml. Twenty-four hours after transduction, 10 mM sodium butyrate was added to boost protein expression and harvested at 72 h. The cell pellet was resuspended in lysis buffer (50 mM Hepes, pH 7.4, 150 mM NaCl, 1 mM DTT, 1%(v/v) EDTA-free protease inhibitor cocktail). Cells were lysed by sonication and protein was extracted in 1.0% (w/v) n-dodecyl-β-d-maltopyranoside (DDM; Anatrace) and 0.1% (w/v) cholesteryl hemisuccinate (CHS) by mild agitation at 4 °C for 3 h. The cell lysate was centrifuged at 40,000 rpm for 60 min, and the supernatant was incubated in amylose resin (New England Biolabs) at 4 °C overnight under gentle agitation. The resin was packed onto a disposable gravity column (Bio-Rad) and washed with ten column volumes of buffer A (50 mM Hepes, pH 7.4, 150 mM NaCl, 0.05% (w/v) glyco-diosgenin (GDN, Anatrace) and 1 mM DTT, 1%(v/v) EDTA-free protease inhibitor cocktail, 0.01 mg/ml soybean lipid), and eluted with four column volumes of buffer B (Buffer A + 40 mM Maltose). All purification procedures were carried out on ice or at 4 °C. The eluted mTRPML2 protein was collected, concentrated, and further purified by size-exclusion chromatography on a Superose 6 10/300 Gl column (GE Heathcare) preequilibrated with buffer C (25 mM Hepes, pH 7.4, 150 mM NaCl, 0.05% (w/v) GDN, and 1 mM DTT, 0.01 mg/mlsoybean polar lipid). The peak fraction corresponding to mTRPML2 was pooled and reconstituted into lipid nanodiscs. Membrane scaffold protein MSP2N2 was expressed in *E. coli* and purified using a tag of hexahistidine(His) in the N terminus. Soybean polar lipid extract (Avanti) dissolved in chloroform was removed from chloroform using nitrogen stream for 10 min. Lipids stock was rehydrated in buffer C by sonication for 10 min and yielded a final concentration of 10 mM. The purified mmTRPML2 sample was mixed with MSP2N2 and the soybean lipid stock at 1:7:300 M ratio, followed by incubate on ice for 30 min. In total, 20 mg/ml Bio-beads SM2 (Bio-Rad) was added to remove additional detergents and initiate lipid nanodiscs reconstitution at 4 °C for overnight with gentle rotation. Bio-Beads were removed *via* disposable gravity column. The reconstitution mixture was centrifuged for 20 min at 4 °C and further purified on a Superose 6 10/300 Gl column in buffer D

Cryo-EM structure of mouse TRPML2 in lipid nanodiscs

(25 mM Hepes, pH 7.4, 150 mM NaCl). The peak corresponding to tetrameric mmTRPML2 reconstituted in lipid nanodisc was collected for analysis by 10% SDS-PAGE, negative stain, and cryo-EM.

EM data acquisition and analysis

The nanodisc-reconstituted mmTRPML2 protein was concentrated to 2.5 mg/ml. A mTRPML2 protein sample volume of 4 μl was applied to a glow-discharged Quantifoil Au R1.2/1.3 holey carbon 400-mesh copper grids. Grids were blotted for 3s at 8 °C and 100% humidity, plunge in liquid ethane, and flash frozen using a Thermo Fisher Vitrobot Mark IV plunger. The cryo-EM samples were collected by a Thermo Fisher Titan Krios G3i microscope operated at 300-kV accelerating voltage. Image stacks were recorded on a Gatan K3 direct detector set in super-resolution counting mode. The data collection was recorded with the semiautomated and low-dose acquisition program EPU (FEI). A calibrated magnification of 640,00× was used for imaging and digital micrograph with defocus range of −1 to −2.5 μm. A total of 6232 micrographs were collected with a pixel size (super resolution) of 0.54 Å. The total dose, 32 e/Å2, was acquired by use of a dose rate of 1.56 e/Å2. Each movie contains 32 frames over 2.56 s total exposure time.

Imaging processing and 3D reconstruction

All cryo-EM data processing was performed by using CryoSparc2.15 (Structura Biotechnology Inc), except local 3D classification, which was done by using Relion3.1 (51). UCSF Chimera (52) was used for visualization, structure segmentation, and determination of the threshold values used to create masks. Software was maintained by Single Particle LLC. Initial movie processing, micrograph screening, template-based particle picking, particle selection, and initial 3D reconstruction were done by using CryoSparc 2.15. In brief, 6387 super-resolution movie stacks were gain normalized and binned 2 × 2 to a pixel size of 1.08 Å by using patch motion correction. Patch CTF estimation was used to check the defocus and max resolution of all the micrographs. After selecting 6232 good micrographs by using maximum resolution, defocus range, and astigmatism, ~4million particles were automatically picked by using homologous protein TRPML1 (EMDB code 9001) as template(32). After particle extraction, several rounds of 2D classification and *ab initio* reconstruction were performed to remove bad particles. After local motion correction, ~144k good particles were used for nonuniform refinement to produce an initial 3D density map with a masked FSC resolution of 3.31 Å. Then all the good particles were exported to Relion 3.1 by using UCSF pyem for further processing. 3D classification with local mask was done by using Relion 3.1. 3D refinement was performed with particles from CryoSparc to obtain the orientation information of each particle. Local mask of transmembrane domain was generated by using UCSF Chimera. The subsequent 3D classification on all the particles was performed with the local mask of transmembrane, while

the orientation of all the particles was fixed at the value determined from last 3D refinement. In total, 23,096 particles with best 3D density were chosen and exported to CryoSparc. One round of 2D classification was performed to further remove bad particles. ~22k good particles were used for nonuniform refinement to produce the final density map with a masked FSC resolution of 3.14 Å.

Model building and refinement

mmTRPML2 maps were visualized in UCSF Chimera. The cryo-EM structures of TRPML3 (PDB: 5W3S) were used as a reference. The ELD structure was used the crystal structure of TRPML2 as a template (PDB: 6HRR), and then mmTRPML2 was manually rebuilt in COOT (53). Idealized helices and beta strands were placed in the electron density and rigid body refined. Side chains were built adhering to optimal rotamer conformations as exhibited by electron density. Amino acid assignment was achieved mainly on the basis of the defined densities for bulky residues. Finally, real space refinement was performed phenix.real_space_refine (54), and good geometry was assessed by MolProbity (55). Radius along the permeation pathway was calculated using HOLE (56). All figures were made in PyMOL.

Data deposition

Cryo-EM electron density map of the mouse TRPML2 has been deposited in the Electron Microscopy Data Bank: https://www.ebi.ac.uk/pdbe/emdb/ (accession number EMD-30924), and the fitted coordinate has been deposited in the Protein Data Bank, www.pdb.org (PDB ID code 7DYS).

Calcium imaging

Single-cell Ca^{2+} imaging experiments were carried out using Fura-2 AM (Beyotine) as previously described (23, 34, 57). For imaging experiments, the coverslips were mounted on to a perfusion chamber positioned on the movable stage of Nikon Ti-E inverted microscope and perfused with standard bath solution by Vacuum Pump. A selective agonist (ML2-SA1) was predicuted in DMSO and stored as 10 mM stock solutions at −20 °C. Working solutions were prepared directly before using by dilution with standard bath solution to 50 μM. After stimulation with ML2-SA1 for 200s. Fura-2 AM ratios (340/380) were used to monitor changes in cytoplasmic Ca^{2+} upon active effects of ML2-SA1. Images at excitation wavelengths were captured every 5s, and the Fura-2 AM ratio (340/380) fluorescence was measured by a Nikon Ti-E system with the NIS-Elements software. All experiment recordings were repeated three times independently. Data are shown as the mean ± SD, one-way ANOVA test followed by Tukey's post-hoc test, ***indicates $p < 0.001$, ns indicates not significant.

Western blotting analysis

HeLa cells were cultured in Dulbecco's Modified Eagle Medium (DMEM) supplemented with 10% fetal bovine

serum (FBS). TRPML2 plasmids or empty vector were cotransfected with mCherry plasmids (9:1 ratio) using Lipofectamine 2000 (Invitrogen Life Technologies) according to the manufacturer's protocol. Twenty-four hours after transfection, cells were lysed in RIPA Buffer (biosharp) containing 1 mM phenylmethanesulfonyl fluoride (Solarbio). Proteins extracts were resolved by SDS-PAGE electrophoresis and transferred onto polyvinylidene difluoride (PVDF) membranes (biosharp). Membranes were blocked with 5% skimmed in Tris-buffered saline containing 0.1% Tween20 (TBST) for 2 h at room temperature and then incubated with the following specific primary antibodies: anti-β-actin (proteintech) diluted 1:1500, anti-SERCA2 (proteintech) diluted 1:5000 and HRP-conjugated secondary goat-anti-mouse antibody (proteintech). The blots were visualized with enhanced chemiluminescence (ECL) substrate (TIANGEN) and exposed using PMCapture software (Tanon). Densitometric analysis was performed using GIS1D software (Tanon). One representative out of three independent experiments is shown. Statistical analysis scatter plots were showed that all the individual data points and standard deviation (SD), one-way ANOVA test, ns indicates not significant.

Data availability

All data are contained within the manuscript and supporting information or are available from the authors: Jin Zhang (zhangxiaokong@hotmail.com), Jingjing Duan (duan.jingjing@ncu.edu.cn), and Yang Fu (fuy@sustech.edu.cn) upon request.

Abbreviations—The abbreviations used are: EH, extracytosolic helix; ELD, extracytosolic/luminal domain; MBP, maltose-binding protein; MSP, membrane scaffold protein; $PI(3,5)P_2$, phosphatidylinositol 3,5-bisphosphate; TMD, transmembrane domain; TRPML, transient receptor potential mucolipin ion channel; VSLD, voltage sensor-like domain.

References

1. Miedel, M. T., Rbaibi, Y., Guerriero, C. J., Colletti, G., Weixel, K. M., Weisz, O. A., and Kiselyov, K. (2008) Membrane traffic and turnover in TRP-ML1-deficient cells: A revised model for mucolipidosis type IV pathogenesis. *J. Exp. Med.* **205**, 1477–1490
2. Xu, H., and Ren, D. (2015) Lysosomal physiology. *Annu. Rev. Physiol.* **77**, 57–80
3. Dong, X. P., Shen, D., Wang, X., Dawson, T., Li, X., Zhang, Q., Cheng, X., Zhang, Y., Weisman, L. S., Delling, M., and Xu, H. (2010) PI(3,5)P(2) controls membrane trafficking by direct activation of mucolipin Ca(2+) release channels in the endolysosome. *Nat. Commun.* **1**, 38
4. Samie, M., Wang, X., Zhang, X., Goschka, A., Li, X., Cheng, X., Gregg, E., Azar, M., Zhuo, Y., Garrity, A. G., Gao, Q., Slaugenhaupt, S., Pickel, J., Zolov, S. N., Weisman, L. S., *et al.* (2013) A TRP channel in the lysosome regulates large particle phagocytosis via focal exocytosis. *Dev. Cell* **26**, 511–524
5. Garrity, A. G., Wang, W., Collier, C. M., Levey, S. A., Gao, Q., and Xu, H. (2016) The endoplasmic reticulum, not the pH gradient, drives calcium refilling of lysosomes. *Elife* **5**, e15887
6. Vergarajauregui, S., and Puertollano, R. (2008) Mucolipidosis type IV: The importance of functional lysosomes for efficient autophagy. *Autophagy* **4**, 832–834
7. Venkatachalam, K., Wong, C. O., and Zhu, M. X. (2015) The role of TRPMLs in endolysosomal trafficking and function. *Cell Calcium* **58**, 48–56
8. Li, P., Gu, M., and Xu, H. (2019) Lysosomal ion channels as decoders of cellular signals. *Trends Biochem. Sci.* **44**, 110–124
9. Venkatachalam, K., Long, A. A., Elsaesser, R., Nikolaeva, D., Broadie, K., and Montell, C. (2008) Motor deficit in a Drosophila model of mucolipidosis type IV due to defective clearance of apoptotic cells. *Cell* **135**, 838–851
10. Chao, Y. K., Chang, S. Y., and Grimm, C. (2020) Endo-lysosomal cation channels and infectious diseases. *Rev. Physiol. Biochem. Pharmacol.* https://doi.org/10.1007/112_2020_31
11. Chen, C. C., Krogsaeter, E., and Grimm, C. (2020) Two-pore and TRP cation channels in endolysosomal osmo-/mechanosensation and volume regulation. *Biochim. Biophys. Acta Mol. Cell Res.* **1868**, 118921
12. Bargal, R., Avidan, N., Ben-Asher, E., Olender, Z., Zeigler, M., Frumkin, A., Raas-Rothschild, A., Glusman, G., Lancet, D., and Bach, G. (2000) Identification of the gene causing mucolipidosis type IV. *Nat. Genet.* **26**, 118–123
13. Zeevi, D. A., Frumkin, A., Offen-Glasner, V., Kogot-Levin, A., and Bach, G. (2009) A potentially dynamic lysosomal role for the endogenous TRPML proteins. *J. Pathol.* **219**, 153–162
14. Bassi, M. T., Manzoni, M., Monti, E., Pizzo, M. T., Ballabio, A., and Borsani, G. (2000) Cloning of the gene encoding a novel integral membrane protein, mucolipidin-and identification of the two major founder mutations causing mucolipidosis type IV. *Am. J. Hum. Genet.* **67**, 1110–1120
15. Slaugenhaupt, S. A., Acierno, J. S., Jr., Helbling, L. A., Bove, C., Goldin, E., Bach, G., Schiffmann, R., and Gusella, J. F. (1999) Mapping of the mucolipidosis type IV gene to chromosome 19p and definition of founder haplotypes. *Am. J. Hum. Genet.* **65**, 773–778

16. Altarescu, G., Sun, M., Moore, D. F., Smith, J. A., Wiggs, E. A., Solomon, B. I., Patronas, N. J., Frei, K. P., Gupta, S., Kaneski, C. R., Quarrell, O. W., Slaugenhaupt, S. A., Goldin, E., and Schiffmann, R. (2002) The neurogenetics of mucolipidosis type IV. *Neurology* **59**, 306–313

17. Chitayat, D., Meunier, C. M., Hodgkinson, K. A., Silver, K., Flanders, M., Anderson, I. J., Little, J. M., Whiteman, D. A., and Carpenter, S. (1991) Mucolipidosis type IV: Clinical manifestations and natural history. *Am. J. Med. Genet.* **41**, 313–318

18. Flores, E. N., and García-Añoveros, J. (2011) TRPML2 and the evolution of mucolipins. *Adv. Exp. Med. Biol.* **704**, 221–228

19. Curcio-Morelli, C., Zhang, P., Venugopal, B., Charles, F. A., Browning, M. F., Cantiello, H. F., and Slaugenhaupt, S. A. (2010) Functional multimerization of mucolipin channel proteins. *J. Cell Physiol.* **222**, 328–335

20. Nagata, K., Zheng, L., Madathany, T., Castiglioni, A. J., Bartles, J. R., and Garcia-Anoveros, J. (2008) The varitint-waddler (Va) deafness mutation in TRPML3 generates constitutive, inward rectifying currents and causes cell degeneration. *Proc. Natl. Acad. Sci. U. S. A.* **105**, 353–358

21. Remis, N. N., Wiwatpanit, T., Castiglioni, A. J., Flores, E. N., Cantu, J. A., and Garcia-Anoveros, J. (2014) Mucolipin co-deficiency causes accelerated endolysosomal vacuolation of enterocytes and failure-to-thrive from birth to weaning. *PLoS Genet.* **10**, e1004833

22. Sun, L., Hua, Y., Vergarajauregui, S., Diab, H. I., and Puertollano, R. (2015) Novel role of TRPML2 in the regulation of the innate immune response. *J. Immunol.* **195**, 4922–4932

23. Plesch, E., Chen, C. C., Butz, E., Scotto Rosato, A., Krogsaeter, E. K., Yinan, H., Bartel, K., Keller, M., Robaa, D., Teupser, D., Holdt, L. M., Vollmar, A. M., Sippl, W., Puertollano, R., Medina, D., *et al.* (2018) Selective agonist of TRPML2 reveals direct role in chemokine release from innate immune cells. *Elife* **7**, e39720

24. Morelli, M. B., Nabissi, M., Amantini, C., Tomassoni, D., Rossi, F., Cardinali, C., Santoni, M., Arcella, A., Oliva, M. A., Santoni, A., Polidori, C., Mariani, M. P., and Santoni, G. (2016) Overexpression of transient receptor potential mucolipin-2 ion channels in gliomas: Role in tumor growth and progression. *Oncotarget* **7**, 43654–43668

25. Santoni, G., Morelli, M. B., Amantini, C., Nabissi, M., Santoni, M., and Santoni, A. (2020) Involvement of the TRPML mucolipin channels in viral infections and anti-viral innate immune responses. *Front. Immunol.* **11**, 739

26. Cuajungco, M. P., Silva, J., Habibi, A., and Valadez, J. A. (2016) The mucolipin-2 (TRPML2) ion channel: A tissue-specific protein crucial to normal cell function. *Pflugers Arch.* **468**, 177–192

27. Chen, C. C., Krogsaeter, E., Butz, E. S., Li, Y., Puertollano, R., Wahl-Schott, C., Biel, M., and Grimm, C. (2020) TRPML2 is an osmo/mechanosensitive cation channel in endolysosomal organelles. *Sci. Adv.* **6**, eabb5064

28. Hirschi, M., Herzik, M. A., Jr., Wie, J., Suo, Y., Borschel, W. F., Ren, D., Lander, G. C., and Lee, S. Y. (2017) Cryo-electron microscopy structure of the lysosomal calcium-permeable channel TRPML3. *Nature* **550**, 411–414

29. Zhou, X., Li, M., Su, D., Jia, Q., Li, H., Li, X., and Yang, J. (2017) Cryo-EM structures of the human endolysosomal TRPML3 channel in three distinct states. *Nat. Struct. Mol. Biol.* **24**, 1146–1154

30. Schmiege, P., Fine, M., Blobel, G., and Li, X. (2017) Human TRPML1 channel structures in open and closed conformations. *Nature* **550**, 366–370

31. Chen, Q., She, J., Zeng, W., Guo, J., Xu, H., Bai, X. C., and Jiang, Y. (2017) Structure of mammalian endolysosomal TRPML1 channel in nanodiscs. *Nature* **550**, 415–418

32. Fine, M., Schmiege, P., and Li, X. (2018) Structural basis for PtdInsP2-mediated human TRPML1 regulation. *Nat. Commun.* **9**, 4192

33. Viet, K. K., Wagner, A., Schwickert, K., Hellwig, N., Brennich, M., Bader, N., Schirmeister, T., Morgner, N., Schindelin, H., and Hellmich, U. A. (2019) Structure of the human TRPML2 ion channel extracytosolic/lumenal domain. *Structure* **27**, 1246–1257.e5

34. Zhong, X. Z., Yang, Y., Sun, X., and Dong, X. P. (2017) Methods for monitoring Ca(2+) and ion channels in the lysosome. *Cell Calcium* **64**, 20–28

35. Shen, P. S., Yang, X., DeCaen, P. G., Liu, X., Bulkley, D., Clapham, D. E., and Cao, E. (2016) The structure of the polycystic kidney disease channel PKD2 in lipid nanodiscs. *Cell* **167**, 763–773.e11

36. Li, M., Zhang, W. K., Benvin, N. M., Zhou, X., Su, D., Li, H., Wang, S., Michailidis, I. E., Tong, L., Li, X., and Yang, J. (2017) Structural basis of dual Ca(2+)/pH regulation of the endolysosomal TRPML1 channel. *Nat. Struct. Mol. Biol.* **24**, 205–213

37. Paulsen, C. E., Armache, J. P., Gao, Y., Cheng, Y., and Julius, D. (2015) Structure of the TRPA1 ion channel suggests regulatory mechanisms. *Nature* **525**, 552

38. Cao, E., Liao, M., Cheng, Y., and Julius, D. (2013) TRPV1 structures in distinct conformations reveal activation mechanisms. *Nature* **504**, 113–118

39. Zubcevic, L., Herzik, M. A., Jr., Chung, B. C., Liu, Z., Lander, G. C., and Lee, S. Y. (2016) Cryo-electron microscopy structure of the TRPV2 ion channel. *Nat. Struct. Mol. Biol.* **23**, 180–186

40. Fine, M., Li, X., and Dang, S. (2020) Structural insights into group II TRP channels. *Cell Calcium* **86**, 102107

41. Feng, X., Huang, Y., Lu, Y., Xiong, J., Wong, C. O., Yang, P., Xia, J., Chen, D., Du, G., Venkatachalam, K., Xia, X., and Zhu, M. X. (2014) Drosophila TRPML forms PI(3,5)P2-activated cation channels in both endolysosomes and plasma membrane. *J. Biol. Chem.* **289**, 4262–4272

42. Xia, Z., Wang, L., Li, S., Tang, W., Sun, F., Wu, Y., Miao, L., and Cao, Z. (2020) ML-SA1, a selective TRPML agonist, inhibits DENV2 and ZIKV by promoting lysosomal acidification and protease activity. *Antiviral Res.* **182**, 104922

43. Di Paola, S., Scotto-Rosato, A., and Medina, D. L. (2018) TRPML1: The Ca$^{(2+)}$retaker of the lysosome. *Cell Calcium* **69**, 112–121

44. Zhang, X., Li, X., and Xu, H. (2012) Phosphoinositide isoforms determine compartment-specific ion channel activity. *Proc. Natl. Acad. Sci. U. S. A.* **109**, 11384–11389

45. Grimm, C., Cuajungco, M. P., van Aken, A. F., Schnee, M., Jörs, S., Kros, C. J., Ricci, A. J., and Heller, S. (2007) A helix-breaking mutation in TRPML3 leads to constitutive activity underlying deafness in the varitint-waddler mouse. *Proc. Natl. Acad. Sci. U. S. A.* **104**, 19583–19588

46. Grimm, C., Jors, S., Guo, Z., Obukhov, A. G., and Heller, S. (2012) Constitutive activity of TRPML2 and TRPML3 channels versus activation by low extracellular sodium and small molecules. *J. Biol. Chem.* **287**, 22701–22708

47. Samie, M. A., Grimm, C., Evans, J. A., Curcio-Morelli, C., Heller, S., Slaugenhaupt, S. A., and Cuajungco, M. P. (2009) The tissue-specific expression of TRPML2 (MCOLN-2) gene is influenced by the presence of TRPML1. *Pflugers Arch.* **459**, 79–91

48. Dong, X. P., Cheng, X., Mills, E., Delling, M., Wang, F., Kurz, T., and Xu, H. (2008) The type IV mucolipidosis-associated protein TRPML1 is an endolysosomal iron release channel. *Nature* **455**, 992–996

49. Lev, S., Zeevi, D. A., Frumkin, A., Offen-Glasner, V., Bach, G., and Minke, B. (2010) Constitutive activity of the human TRPML2 channel induces cell degeneration. *J. Biol. Chem.* **285**, 2771–2782

50. Xu, H., Delling, M., Li, L., Dong, X., and Clapham, D. E. (2007) Activating mutation in a mucolipin transient receptor potential channel leads to melanocyte loss in varitint-waddler mice. *Proc. Natl. Acad. Sci. U. S. A.* **104**, 18321–18326

51. Zivanov, J., Nakane, T., Forsberg, B. O., Kimanius, D., Hagen, W. J., Lindahl, E., and Scheres, S. H. (2018) New tools for automated high-resolution cryo-EM structure determination in RELION-3. *Elife* **7**, e42166

52. Pettersen, E. F., Goddard, T. D., Huang, C. C., Couch, G. S., Greenblatt, D. M., Meng, E. C., and Ferrin, T. E. (2004) UCSF Chimera—a visualization system for exploratory research and analysis. *J. Comput. Chem.* **25**, 1605–1612

53. Emsley, P., Lohkamp, B., Scott, W. G., and Cowtan, K. (2010) Features and development of Coot. *Acta Crystallogr. D Biol. Crystallogr.* **66**, 486–501

54. Afonine, P. V., Grosse-Kunstleve, R. W., Echols, N., Headd, J. J., Moriarty, N. W., Mustyakimov, M., Terwilliger, T. C., Urzhumtsev, A., Zwart, P. H., and Adams, P. D. (2012) Towards automated crystallographic structure refinement with phenix.refine. *Acta Crystallogr. D Biol. Crystallogr.* **68**, 352–367

55. Chen, V. B., Arendall, W. B., 3rd, Headd, J. J., Keedy, D. A., Immormino, R. M., Kapral, G. J., Murray, L. W., Richardson, J. S., and Richardson, D. C. (2010) MolProbity: All-atom structure validation for macromolecular crystallography. *Acta Crystallogr. D Biol. Crystallogr.* **66**, 12–21

56. Smart, O. S., Neduvelil, J. G., Wang, X., Wallace, B. A., and Sansom, M. S. (1996) Hole: A program for the analysis of the pore dimensions of ion channel structural models. *J. Mol. Graph.* **14**, 354–360, 376

57. Duan, J., Li, J., Zeng, B., Chen, G. L., Peng, X., Zhang, Y., Wang, J., Clapham, D. E., Li, Z., and Zhang, J. (2018) Structure of the mouse TRPC4 ion channel. *Nat. Commun.* **9**, 3102